Anal Bioanal Chem (2012) 404:1287–1296
DOI 10.1007/s00216-012-6217-y

ORIGINAL PAPER

X-ray microscopy and tomography detect the accumulation of bare and PEG-coated gold nanoparticles in normal and tumor mouse tissues

C-C. Chien · C-C. Cheng · H. H. Chen · Y. Hwu · Y. S. Chu · C. Petibois · A. Chen · Y-T. Ching · G. Margaritondo

Received: 9 February 2012 / Revised: 23 May 2012 / Accepted: 20 June 2012 / Published online: 20 July 2012

Abstract We demonstrate that, with appropriate staining, high-resolution X-ray microscopy can image complicated tissue structures—cerebellum and liver—and resolve large or small amounts of Au nanoparticles in these tissues. Specifically, images of tumor tissue reveal high concentrations of accumulated Au nanoparticles. PEG (poly(ethylene glycol)) coating is quite effective in enhancing this accumulation and significantly modifies the mechanism of uptake by reticuloendothelial system (RES) organs.

Keywords High resolution X-ray microscopy · Nanoparticles · 3D tissue imaging

Introduction

Potential applications of nanoparticles to drug delivery [1–3], image contrast enhancement [2, 4–6] and radiation therapy [7–9] require effective experimental methods to study their behavior. Imaging techniques can be very effective, if they have sufficient spatial resolution and sensitivity [10–16]. Special nanoparticles are already used for specific imaging methods, e.g., as fluorescent dyes [17, 18], radioisotope tracers [19], contrast agents for magnetic resonance imaging [20–22], and other approaches [20, 23–25]. The common requirement for all of these is to be easily located

Published in the special paper collection *Imaging Techniques with Synchrotron Radiation* with guest editor Cyril Petibois.

C.-C. Chien · H. H. Chen · Y. Hwu
Institute of Physics, Academia Sinica,
Nankang,
Taipei 115, Taiwan

C.-C. Chien · Y. Hwu
Department of Engineering and System Science,
National Tsing Hua University,
Hsinchu 300, Taiwan

C.-C. Cheng · Y.-T. Ching
Department of Computer Science,
National Chiao Tung University,
Hsinchu 300, Taiwan

Y. Hwu (✉)
Advanced Optoelectronic Technology Center,
National Cheng Kung University,
Tainan 701, Taiwan
e-mail: phhwu@sinica.edu.tw

Y. Hwu
e-mail: phhwu@sinica.edu.tw

Y. S. Chu
National Synchrotron Light Source-II,
Brookhaven National Laboratory,
Upton, NY 11973-5000, USA

C. Petibois
CNRS UMR 5248, CBMN, University of Bordeaux,
33600, Pessac-Cedex, France

A. Chen
Division of Experimental Pathology, Tri-Service General Hospital,
Taipei 114, Taiwan

G. Margaritondo
Ecole Polytechnique Fédérale de Lausanne (EPFL),
1015 Lausanne, Switzerland

Table 1 Contrast agents and their concentrations used in this study

Stain	Concentration
Potassium permanganate ($KMnO_4$)	1 % (*w*/*w*) in distilled water
Phosphotungstic acid (PTA)	1 % (*w*/*w*) in distilled water
Iodine–potassium iodide (IKI)	1 % (*w*/*w*) in distilled water
Osmium tetroxide (OsO_4)	2 % (*w*/*w*) in distilled water

and traced. Ideally, they should also be multifunctional, having a biological or biomedical purpose: this, however, is difficult to achieve.

Here, we exploit the strong X-ray absorption of Au nanoparticle (AuNP) systems to microscopically image their accumulation in mice. Note that AuNPs are quite biocompatible and have many promising biomedical applications [8, 26–31].

We specifically focus our attention on a key issue of nanomedicine: passive AuNP accumulation by tumor tissues, attributed to the "enhanced permeation and retention (EPR)" effect [32–35]. We investigate both bare-AuNPs and PEG-AuNPs (poly(ethylene glycol) (PEG)-coated) and compare their distribution in lung, liver, spleen, kidney, and tumor tissues. The results specifically show that the PEG coating modifies AuNP uptake by these tissues, reducing their accumulation in lung, liver, and spleen and increasing the concentration in tumors. We thus confirm the conclusions of organ-level distribution studies [36–39], but provide a more detailed microscopic picture of the uptake mechanisms explaining how PEG coating enhances accumulation by tumors.

Appropriate staining is crucial to obtaining high-resolution X-ray tissue images with subcellular details [10, 29]. We developed an ad-hoc staining method based on potassium permanganate ($KMnO_4$) [40, 41] and demonstrate here that it reveals finer details than other heavy-metal staining methods commonly used for transmission electron microscopy (TEM). This test also indicated that because of different specimen thickness and the strength of absorption contrast, the staining methods cannot be automatically adopted from TEM. With $KMnO_4$ staining, the increased image contrast does not negatively affect the sensitivity of detection of AuNPs in tissues.

We use this staining method with a full-field zone-plate X-ray microscope with nanometer resolution; this is adequate for imaging nanoparticles and their aggregates in thick specimens and in three dimensions (3D) and for identifying their location at the subcellular level in different organs. This approach specifically enables us to reach the aforementioned conclusions about the effects of PEG coating.

Our approach is not limited to small and/or thin specimens and can be applied to other inorganic nanoparticles. Therefore, it can be specifically used to develop nanoparticle coatings optimized for different applications.

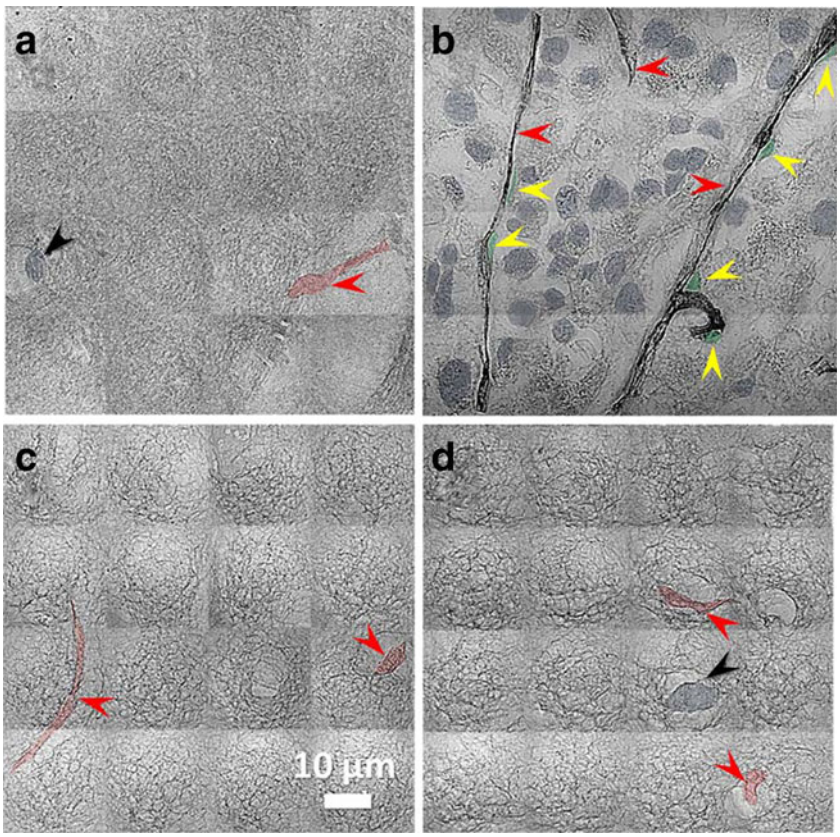

Fig. 1 X-ray micrographs of cerebral tissue with different stains: (**a**) OsO_4, (**b**) $KMnO_4$, (**c**) IKI, and (**d**) PTA. With $KMnO_4$, individual cells and blood vessels (*red arrowheads*) can be identified. We can also identify the endothelial cell nuclei (*yellow arrowheads*). In contrast, in (a), (c), and (d) it is difficult to differentiate individual cells (*black arrowheads*), vessels (*red arrowheads*), and the extracellular matrix (ECM). The tissues for (b), (c), and (d) were perfused with AuNP colloidal solution to increase the visibility of the vasculature. However, the vessels can be clearly identified only in (b). Overall, these results identify $KMnO_4$ as the best staining agent for vasculature imaging

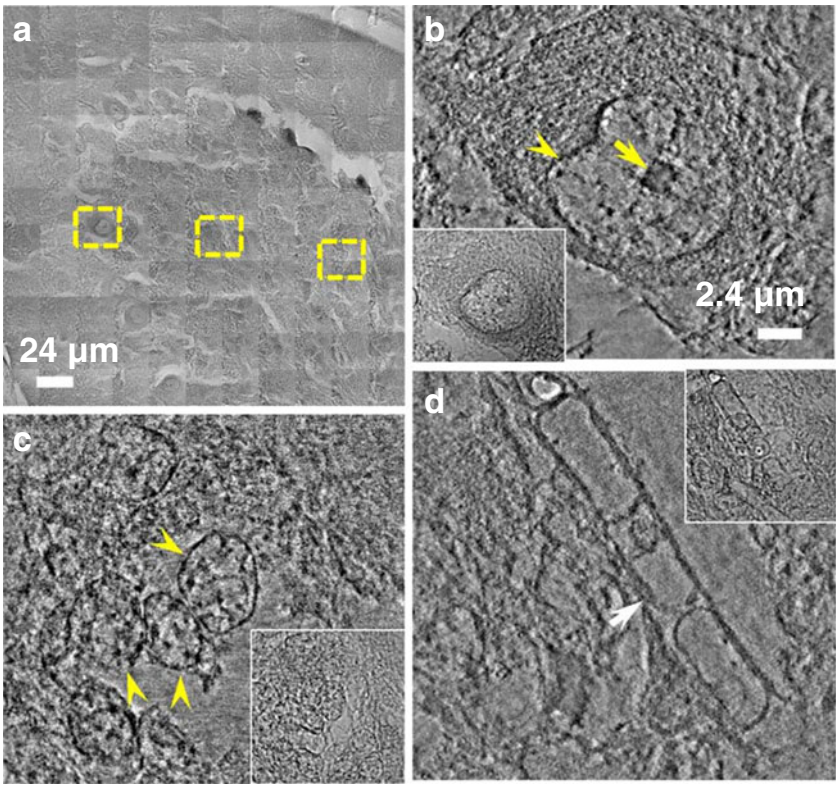

Fig. 2 X-ray micrographs of cerebellum tissues stained with $KMnO_4$. (**a**) Patched image; the *yellow squares* correspond to the other three images, which are tomography-reconstructed slices of Purkinje cells (**b**), cerebellar granule cells (**c**), and myelin sheath (**d**). Dense cytoplasm, and nucleolus and chromatins in the nucleus are clearly visible. The *arrow* in (b) marks the nucleolus and the *arrowhead* the nuclear membrane. The *arrowheads* in (c) mark the nucleus. The *arrow* in (d) marks the myelin sheath. *Scale bars*: (a), 24 μm; (b), (c), and (d), 2.4 μm

Experimental

Preparation of the test tissue specimens

The Academia Sinica Institutional Animal Care and Utilization Committee (AS IACUC) approved all animal experiments. We purchased BALB/c mice from the National Laboratory Animal Center, Taiwan and housed them in individually ventilated cages (five per cage) with wood chip bedding, kept at 24± 2 °C with 40–70 % humidity and a 12-hour light–dark cycle. The subcutaneous tissue of the left leg region was inoculated with EMT cells (1×10^7 cells mL^{-1}) in 50 μL Matrigel (BD Biosciences) for 7 days to induce the development of subcutaneous tumors. The tumor volume was defined as $v=0.5\times a\times b^2$, where a and b are the largest and the smallest diameters. We performed the imaging experiments after the tumor developed to a size of 100–120 mm^3, by injecting 200 μL AuNP solution via the tail vein, or by locally injecting 10 μL (10 mg mL^{-1}) AuNP solution three times at the tumor site for each mouse.

Two kinds of nanoparticle, bare AuNPs (10 mg mL^{-1}) [42, 43] and PEG-AuNPs (26 mg mL^{-1}) [28, 44], were separately injected (200 μL each) into the tail vein. After 24 h, the mice were sacrificed. Tumor, lung, liver, kidney, and spleen tissues were removed, immersed in 3.7 % paraformaldehyde for 24 h, then washed three times with PBS (phosphate buffer solution) for 1 h.

Tissue specimens were dehydrated, embedded in paraffin, and sliced to a thickness ~10–30 μm. We removed the remaining paraffin by immersion in xylene for 5 min. After triple washing, the samples were rehydrated, immersed in distilled water and stained with a 1 % *w*/*w*) solution of potassium permanganate ($KMnO_4$). For comparison, some samples were stained with 2 % Osmium tetroxide (OsO_4), 1 % phosphotungstic acid (PTA), or mixed iodine metal and potassium iodide (iodine–potassium iodide, IKI) [45]. Some of the specimens with nanoparticles were also treated by hematoxylin and eosin (H&E) staining. All specimens were then washed three times with distilled water for 10 min and dehydrated again with increasing ethanol concentrations. Finally, the specimens were embedded in Embed-812 Resin (EMS, Hatfield, PA, USA). The staining agents and the corresponding concentrations are summarized in Table 1.

High-resolution X-ray imaging

We performed the tests on the 32-ID-D beamline of the Advanced Photon Source (APS, Argonne) and on the 01B beamline of the National Synchrotron Radiation Research Center (NSRRC, Taiwan). The full-field high-resolution X-ray microscope includes several optical components: capillary lenses, zone plates, phase rings [12], and others. Capillary lenses acts as condensers providing illumination that fits the object, with numerical aperture matched to the zone plate, which can be selected from a set according to experimental requirements. A monochromatic (8 keV photon energy) X-ray flux of 2×10^{11} photons s^{-1} was obtained with a Si (111)

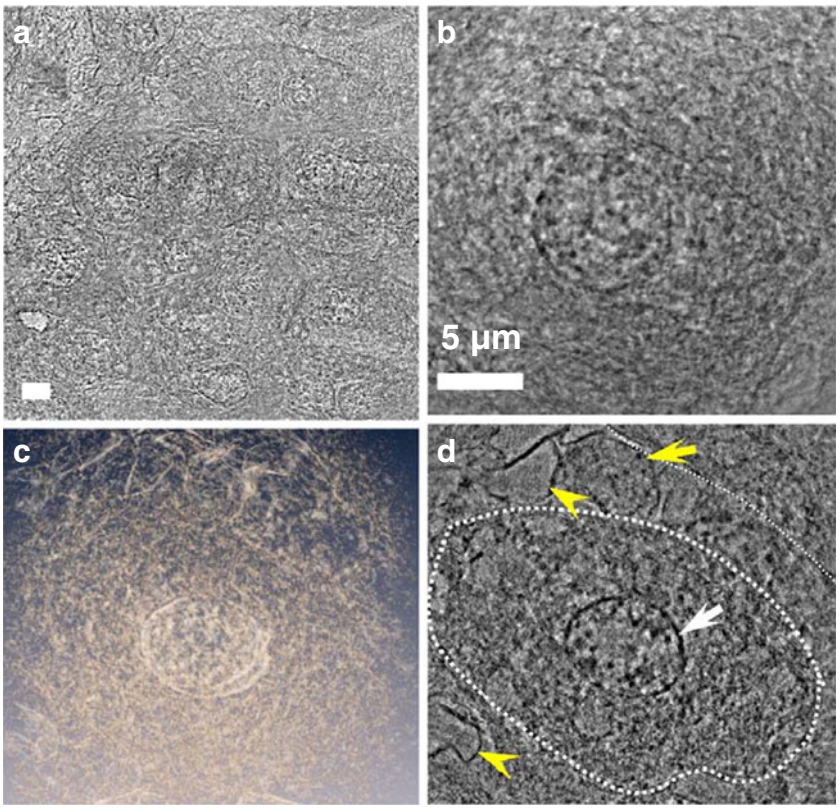

Fig. 3 X-ray micrographs of liver tissue: (**a**) patched image; (**b**) projection image; (**c**) reconstructed tomographic image; (**d**) reconstructed single-slice image. The *yellow arrowheads* and *arrow* mark red blood cells and a cell with its nucleus. The *white arrow* marks the nucleus of a hepatocyte. *Scale bars*: 5 μm

double crystal monochromator. Zernike phase contrast imaging could be implemented with an Au phase ring placed at the back focal plane of the Fresnel zone plate [46]. The microscope could deliver images with a 50 ms per frame exposure

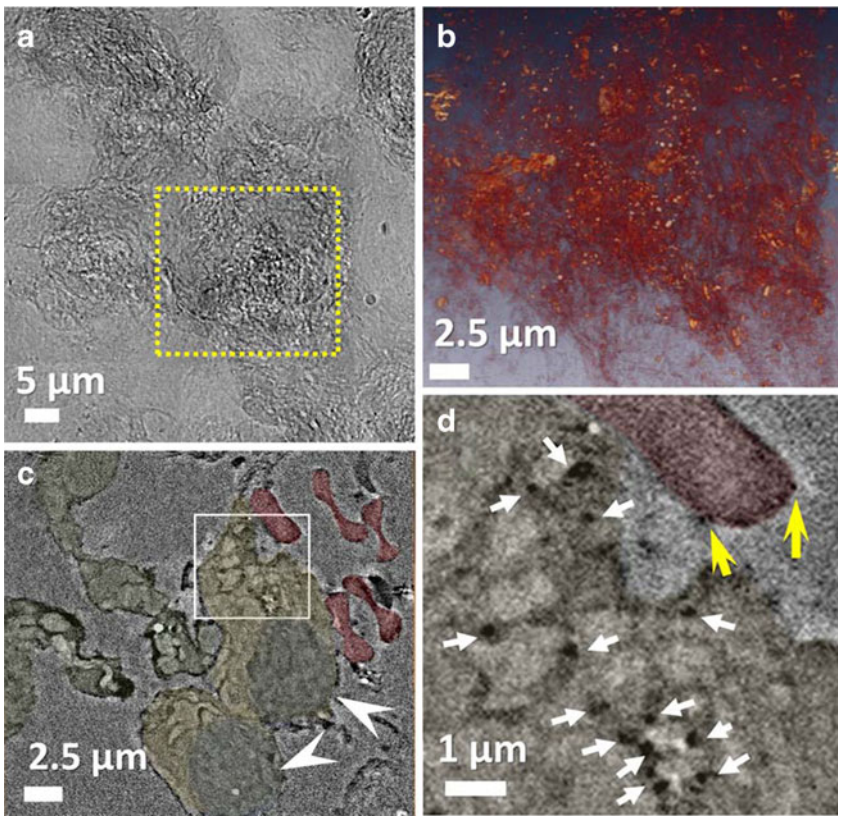

Fig. 4 X-ray micrographs of lung tissue after exposure to bare-AuNPs for 24 h: (**a**) patch image; (**b**) tomographic reconstructed image of the *yellow square* in (a); the 60–200 nm golden dots are aggregates of bare-AuNPs. (**c**) Single-slice tomographic reconstructed image of (b); the *arrowheads* mark the nuclei (darker regions) of two alveolar cells. (**d**) Magnified view of the *white square* in (c). *Yellow arrows* mark bare-AuNPs aggregates attached to red blood cell surfaces and *white arrows* mark bare-AuNPs located inside alveolar cells. *Scale bars*: (a), 5 μm; (b) and (c), 2.5 μm; (d), 1 μm

yielding ~1×10^4 counts per pixel at the charge-coupled device detector. The total magnification of the zone-plate plus the visible light imaging system was 900–2400×. The selected photon energy of 8 keV simultaneously optimized the zone plate effectiveness and the contrast [12–14, 46, 47]. Tomography reconstructions were performed starting from 160 or 320 projection images taken at 0.5 or 1-degree intervals. A comprehensive description of the experimental setup and a discussion of the capabilities of TXM (transmission X-ray microscopy) when applied to different types of biological specimens can be found in Ref. [48].

Results and discussion

We first show that staining based on $KMnO_4$ produced clear images at the cellular level for tissues. Figure 1 is a set of high-resolution X-ray micrographs of cerebral tissues with different types of staining: OsO_4, $KMnO_4$, IKI, and PTA [45]. OsO_4 is known to stain unsaturated lipids, proteins, and lipoprotein membranes; Fig. 1a shows the corresponding results for the dense structure of the cell nucleus, the cytoplasm, and the extracellular matrix in the cerebral tissue. Figure 1b shows the results of $KMnO_4$ staining, which was found to be deposited on the membrane surfaces in the form of dense precipitates, providing high visibility for small features. In comparison, with IKI and PTA (Fig. 1c and d) only extracellular components, for example elastin, collagen, and basement membrane, were clearly visible. From these and other results, we concluded that $KMnO_4$ was the best choice.

Figure 2 shows X-ray micrographs of $KMnO_4$-stained mouse cerebellum tissue. Note that molecular layer (M), Purkinje cell layer (P), granular layer (G), and white matter area (W) are clearly distinguishable from each other (Fig. 2a). Purkinje cells have clear boundaries between nuclei and cytoplasm. Large nuclei with nucleolus and nucleus-associated chromatin are clearly visible (Fig. 2b).

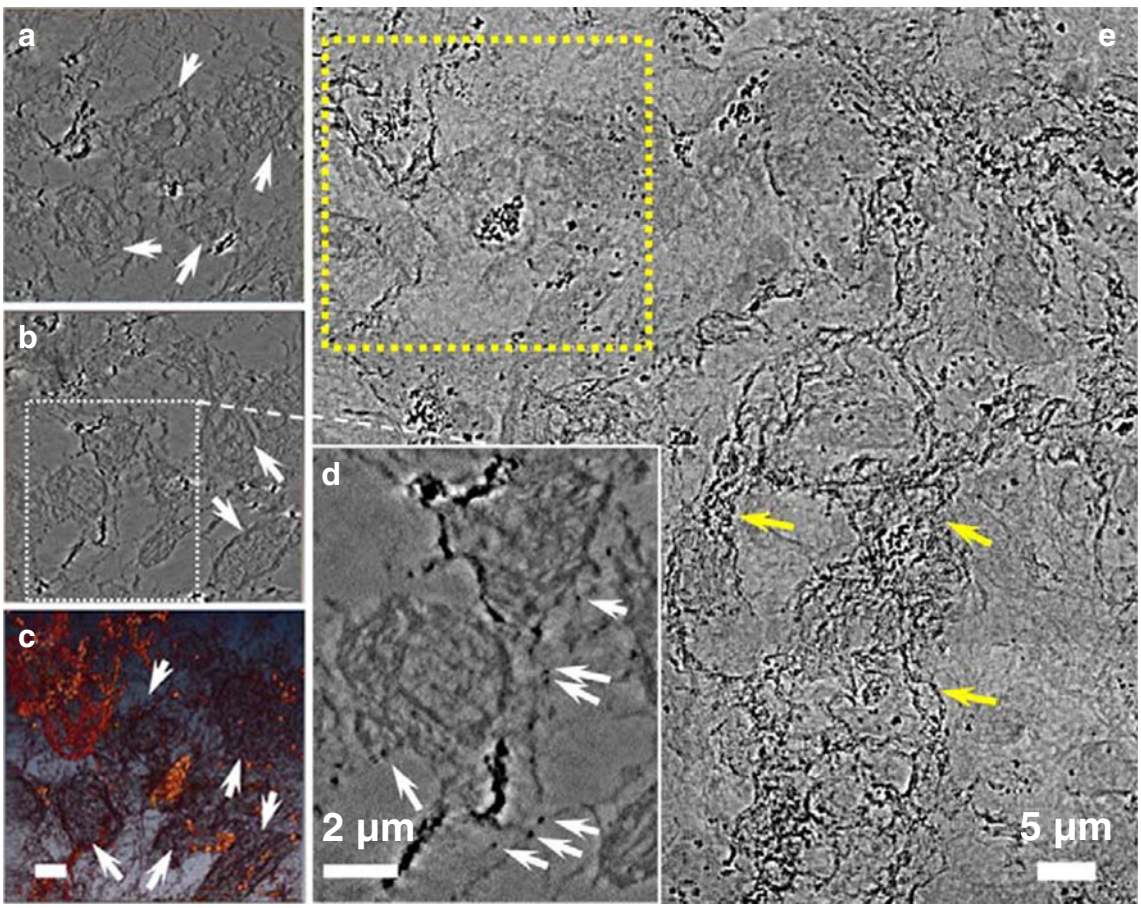

Fig. 5 X-ray micrographs of locally injected bare-AuNPs in subcutaneous tumor (developed by injecting Matrigel mixed with tumor cells). These micrographs show that large amounts of bare-AuNPs are accumulated in the ECM and smaller amounts in cells. (**a**), (**b**), and (**c**) are reconstructed images corresponding to the yellow square in (e). Cell nuclei can be seen in (a), (b), and (c) (e.g., those marked by *white arrows*). The magnified version of the rectangle (b), shown in (**d**), reveals that bare-AuNPs (*white arrows*) are present on the surfaces of two cells; black line shape structures in (e); a few examples marked by *yellow arrows* show bare-AuNPs accumulated in the ECM. (a) and (b) are different sections of (c). (**e**) patched TXM micrographs of tumor tissue after treatment with bare-AuNPs. *Scale bars*: (a), (b), (c), and (d), 2 μm; (e), 5 μm

Cerebellar granule cell nuclei are apparent in Fig. 2c. Myelin sheath can also be identified in the white matter (Fig. 2d).

Figure 3 shows images of a mouse hepatocyte taken from sliced liver tissue with $KMnO_4$ staining. We obtained a 3D tomography reconstruction of this cell with sufficient quality to detect subcellular structures, for example nuclei and cytoplasm. From the morphology, we can distinguish different cell types in these tissue sections. For example, the yellow arrowheads in Fig. 3d mark red blood cells whereas the yellow and white arrows mark the cell and the nucleus (Fig. 3d).

Sub-cellular staining with $KMnO_4$ enabled us to accurately determine the AuNP location in each cell. For example, Fig. 4 shows lung tissue with small bare-AuNP aggregates accumulated after tail-vein injection. Figure 4b is a single-slice image obtained by tomography reconstruction, corresponding to the yellow square in Fig. 4a.

The size of bare-AuNP aggregates, ~60–200 nm, is substantially larger than that of a single bare-AuNP, ~15 nm. These aggregates are clearly visible and mostly located in alveolar cells; quantitative evaluation of their number and size give an Au density of ~7.3 μg mm^{-3}. Note that such a large number of bare-AuNPs in the lung for a long time is not desirable for nanomedicine applications.

We also see in Fig. 5d and e bare AuNPs in subcutaneous tumor. The images show unstable agglomerated nanoparticles adhering to tumor cells and to the extracellular matrix (ECM, Matrigel BD) (Fig. 5d and e). This kind of result is valuable for studying the interaction of AuNPs with tissues.

To avoid undesired accumulation of AuNPs, a well-known strategy is surface coating with polymers, which are inert in the blood and can prolong the nanoparticle presence in the circulation system before being recognition by the RES system. Widely used is PEG [35, 37, 38, 49, 50], a highly hydrophilic polymer that, by means of steric repulsion forces, prevents opsonin proteins from being adsorbed by the nanoparticle surface and impedes recognition by macrophages. PEG-AuNPs remain in the bloodstream for hours, dramatically increasing the effectiveness of accumulation in tumors.

We produced PEG-AuNPs by slight modification of the one-pot synthetic method for bare-AuNPs; it is based on X-ray irradiation and id described in Refs. [28, 42, 43]. Both the bare and PEG-coated AuNPs thus obtained have excellent biocompatibility, colloidal properties, and long-term stability [10, 28, 51]. They can be purified to very high concentrations. The two types of AuNP have different EPR effects [28]. In particular, high accumulation of bare-AuNPs is observed in RES organs, which results in a lower absolute AuNP percentage accumulated at tumor sites (data not shown).

Pharmacokinetic study confirmed that our PEG-AuNPs have a much longer lifetime in blood than their bare counterparts. Their accumulation in tumor, liver, kidney, and spleen tissues steadily increased for a much longer time, up to ~24 h. By use of special Fresnel zone plate objectives with ~20 nm outermost zone width, we could image the corresponding tissues with resolution <20 nm [14, 52]. This was not quite sufficient to detect individual AuNPs (size ~15 nm), but did reveal their aggregates.

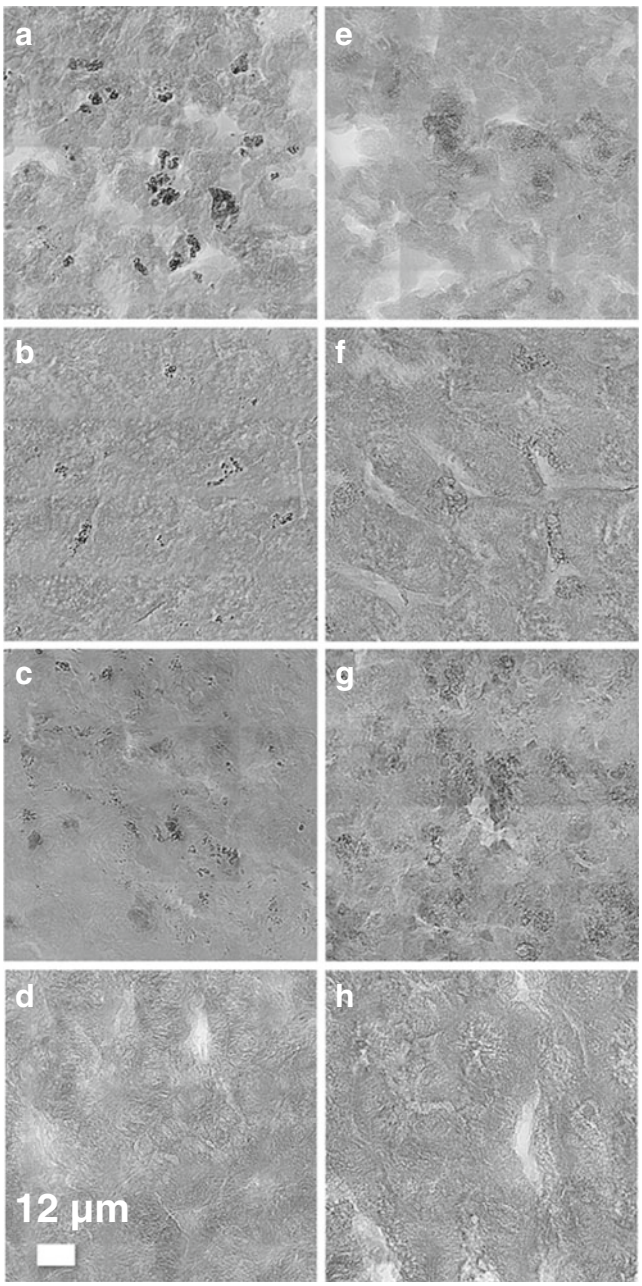

Fig. 6 High-resolution patched TXM micrographs of different tissues after two different AuNP treatments, showing different accumulations. (**a**)–(**d**) correspond to lung, liver, spleen and kidney tissues treated with bare-AuNPs. (**e**)–(**h**) correspond to the same tissues treated with PEG-AuNPs. In (a), (b), and (c), bare-AuNPs aggregate, forming dense gold clusters. In (e) and (h), most PEG-AuNPs form, instead, dark gray hollow circle vesicles in cells. *Scale bar*: 12 μm

Without surface modification, one expects large AuNPs agglomerates, because the lungs can effectively filter them (Fig. 6a). Figure 7a and d show that AuNPs in the lungs form agglomerates with size up to 5–10 μm and block small vessels. The rest of the small AuNPs keep circulating and then accumulate in the spleen and in the liver. Most AuNPs found in these organs form spherical agglomerates.

From TXM images, for example Fig. 6b and c, we estimate particle sizes to be in the 350–450 nm range in the liver and 250–350 nm in the spleen. Figure 7b and e show that in the liver small agglomerated AuNPs are accumulated in Kupffer cells whereas Fig. 7c and f show that in the spleen the nanoparticles are internalized by the red pulp. In contrast, we did not find AuNPs in hepatocytes (marked by arrows in Fig. 7b). This indicates that internalization predominantly occurs in specific types of cell in the liver.

With regard to PEG-AuNPs, we have already mentioned that the coating prolongs the circulation time. We found, however, that it does not completely avoid surface modifications by opsnin protein adhesion: the coated nanoparticles are still recognized by macrophages. In high-resolution X-ray micrographs, PEG-AuNPs were found to be internalized in vesicles, forming hollow circle shapes in cells (Fig. 6e–g). Non-uniform distributions of multi-vesicles in macrophages were only found in the lungs (Fig. 7g and j). Note that this analysis requires imaging large areas and/or volumes without compromising resolution; TXM imaging using large area patchworks seems quite effective in that regard [17].

The PEG-AuNPs vesicle distribution in Kupffer cells (Fig. 7h and k) is between 500 and 1600 nm, whereas in splenic red pulp it is between 900 and 2000 nm (Fig. 7i and l). We cannot, however, rule out the possible presence of non-agglomerated PEG-AuNPs (6.1±1.9 nm) with our ~20 nm resolution [14].

We detected neither bare nor PEG-coated AuNPs in kidney tissues—Fig. 6d and h. The reasons could be the large

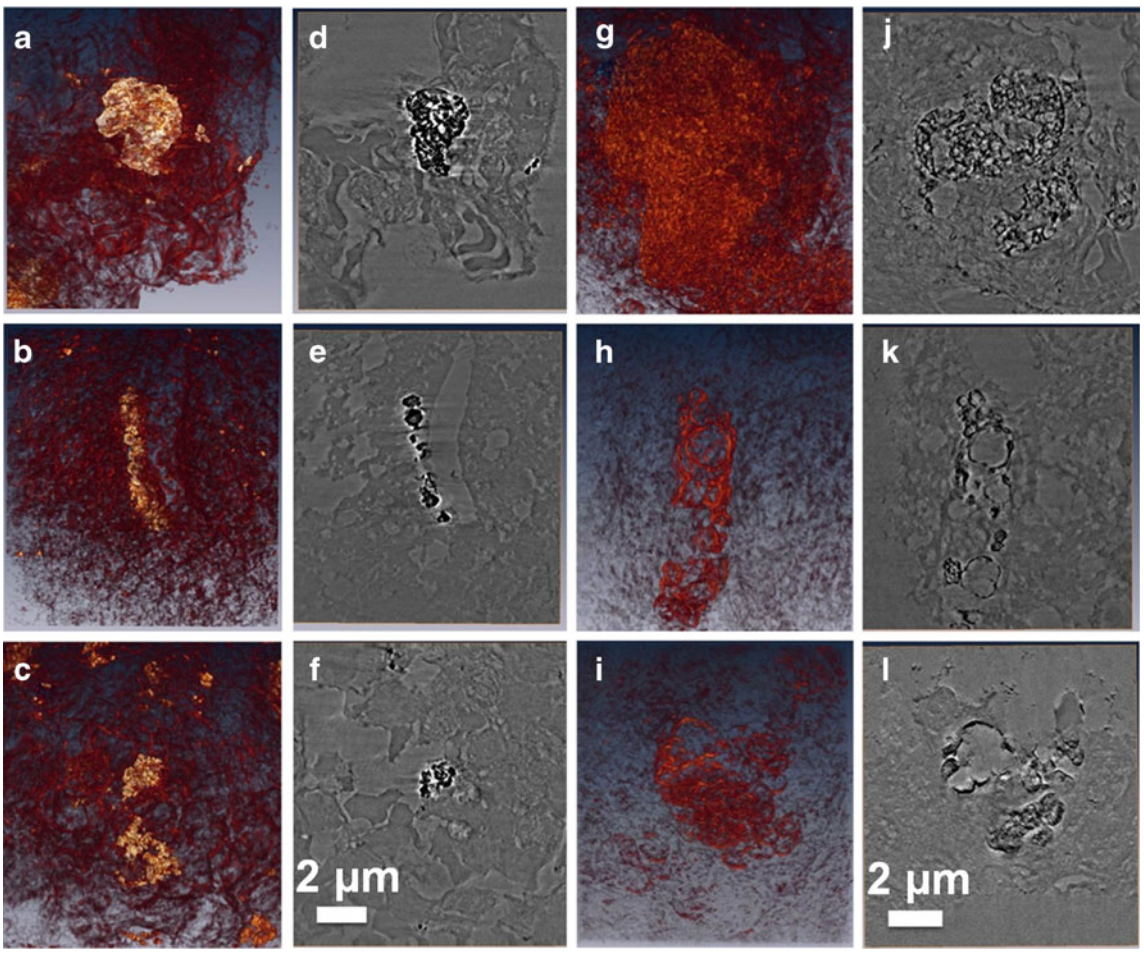

Fig. 7 High-resolution tomography reconstructed micrographs show the accumulation of AuNPs in different tissues. (**a**) to (**c**): 3D reconstructed images for lung (a), liver (b) and spleen (c). The golden color marks dense bare-AuNP clusters whereas the dark red color corresponds to the tissue. (**d**) to (**f**): single-slice images corresponding to (a)–(c), showing the dark, dense bare-AuNP aggregates. (**g**) to (**i**): 3D tomography reconstructed images of lung (g), liver (h), and spleen (i) tissues treated with PEG-AuNPs. The red color marks PEG-AuNPs in the spherical vesicles. (**j**) to (**l**): single-slice images corresponding to (a)-(c), revealing vesicles containing PEG-AuNP. Multi-vesicles (dark hollow vesicles) of PEG-AuNPs are found in the lung tissue (j). *Scale bars*: 2 μm.

amounts of AuNPs sequestered by the RES system and the fact that PEG-AuNPs are not small enough to penetrate the endothelium.

Figure 8 shows an example of AuNP aggregates in tumor tissues. Bare-AuNPs are difficult to detect (Fig. 8a and c–e), whereas PEG-AuNPs are easily observed, showing that they are internalized in tumor cells (Fig. 8b and f–h). This further confirms that the concentration and/or accumulation of bare-AuNPs in tumors is much lower than for PEG-AuNPs. We also found that for PEG-AuNPs small nanoparticle-containing vesicles are distributed from the surface to the cytoplasm (inset in Fig. 8h) within the cells.

Conclusions

We have developed and tested an imaging approach based on ad-hoc staining for high-resolution X-ray microscopy that enables direct visualization, at sub-cellular level, of AuNP internalization in different tissues. Specifically, we demonstrated that with $KMnO_4$ staining high-resolution X-ray microscopy can resolve dense and complicated sub-cellular features in tissue specimens and provide important qualitative and quantitative information about nanoparticle internalization processes.

This led to verification that PEG-AuNPs accumulate strongly in tumors and shed new light on the differences between bare and PEG-coated AuNPs. For example, we clarified the mechanisms underlying previous results for tumor accumulation and cell internalization of PEG-AuNPs compared with bare-AuNPs. Specifically, we showed that the higher absolute concentration of PEG-AuNPs in tumors is a direct consequence of the PEG coating, which prolongs circulation in the bloodstream and increases the possibility of reaching a tumor.

These results prove the feasibility of our method, including quantitative evaluation. They also show its effectiveness and flexibility compared with other approaches, which do not have

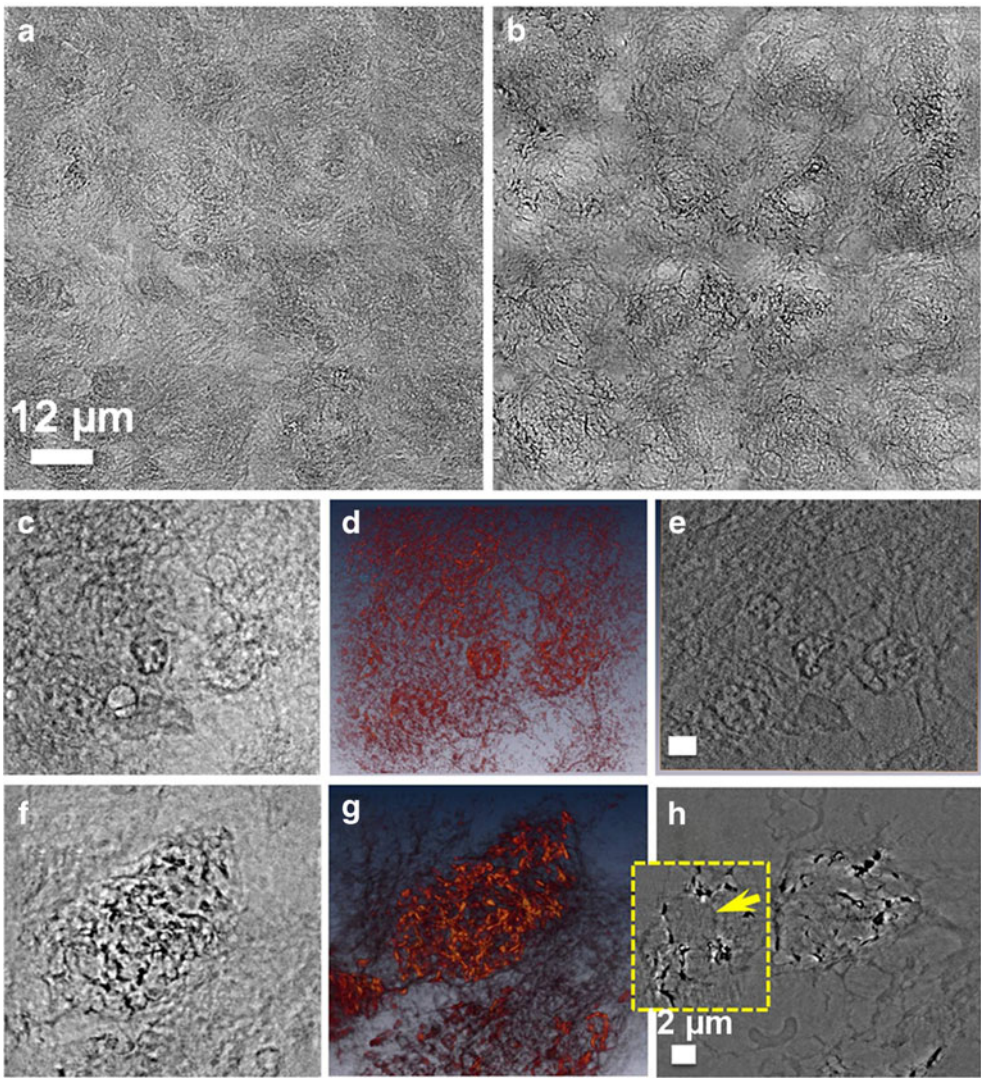

Fig. 8 TXM micrographs of tumor tissues after treatment with bare-AuNPs and PEG-AuNPs. Smaller amounts of bare-AuNPs (a) accumulated in tumors than of PEG-AuNPs (b). PEG-AuNPs were found in small vesicles (light red in (g) and black dots in (h)) in tumor cells. The inset in (h) shows the cell nucleus (*arrow*) and small vesicles (black dots). (**a**) and (**c**) are projection micrographs of tumor tissue after bare-AuNPs treatment whereas (**b**) and (**f**) are projection micrographs after PEG-AuNPs treatment. (**d**) and (**g**) are tomographic reconstructed images corresponding to (c) and (f). (**e**) and (**h**) are single-slice images corresponding to (d) and (g). *Scale bars*: (a) and (b), 12 μm; all other images, 2 μm

sufficient resolution to directly image AuNPs (or AuNP aggregates), or cannot penetrate large tissue specimens.

References

1. Kim D, Jeong YY, Jon S (2010) A drug-loaded aptamer-gold nanoparticle bioconjugate for combined CT imaging and therapy of prostate cancer. ACS Nano 4:3689–3696
2. Rothenfluh DA, Bermudez H, O'Neil CP, Hubbell JA (2008) Biofunctional polymer nanoparticles for intra-articular targeting and retention in cartilage. Nat Mater 7:248–254
3. Prabaharan M, Grailer JJ, Pilla S, Steeber DA, Gong S (2009) Gold nanoparticles with a monolayer of doxorubicin-conjugated amphiphilic block copolymer for tumor-targeted drug delivery. Biomaterials 30:6065–6075
4. Popovtzer R, Agrawal A, Kotov NA, Popovtzer A, Balter J, Carey TE, Kopelman R (2008) Targeted Gold Nanoparticles Enable Molecular CT Imaging of Cancer. Nano Lett 8:4593–4596
5. Chien CC, Kempson IM, Wang CL, Chen HH, Hwu Y, Chen NY, Lee TK, Petibois C, Tsai KK, Liu MS, Chang KY, Yang CS, Margaritondo G (2011) Complete microscale profiling of tumor microangiogenesis A microradiological methodology reveals fundamental aspects of tumor angiogenesis and yields an array of quantitative parameters for its characterization. Biotechnol Adv. doi:10.1016/j.biotechadv.2011.12.001
6. Chien CC, Wang CH, Wang CL, Li ER, Lee KH, Hwu Y, Lin CY, Chang SJ, Yang CS, Petibois C, Margaritondo G (2010) Synchrotron microangiography studies of angiogenesis in mice with microemulsions and gold nanoparticles. Anal Bioanal Chem 397:2109–2116
7. Au L, Chen J, Wang LV, Xia Y (2010) Gold nanocages for cancer imaging and therapy. Methods Mol Biol 624:83–99
8. Brannon-Peppas L, Blanchette JO (2004) Nanoparticle and targeted systems for cancer therapy. Adv Drug Deliv Rev 56:1649–1659
9. Chien CC, Wang CH, Hua TE, Tseng PY, Yang TY, Hwu Y, Chen YJ, Chung KH, Je JH, Margaritondo G (2007) Synchrotron x-ray synthesized gold nanoparticles for tumor therapy. In: Choi JY, Rah S (eds) Synchrotron Radiation Instrumentation, Pts 1 and 2, vol 879. AIP Conference Proceedings. American Institute of Physics, New York, pp 1908–1911
10. Chen HH, Chien CC, Petibois C, Wang CL, Chu YS, Lai SF, Hua TE, Chen YY, Cai X, Kempson IM, Hwu Y, Margaritondo G (2011) Quantitative analysis of nanoparticle internalization in mammalian cells by high resolution X-ray microscopy. J Nanobiotechnology 9:14
11. Chu YS, Yi JM, De Carlo F, Shen Q, Lee WK, Wu HJ, Wang CL, Wang JY, Liu CJ, Wang CH, Wu SR, Chien CC, Hwu Y, Tkachuk A, Yun W, Feser M, Liang KS, Yang CS, Je JH, Margaritondo G (2008) Hard-x-ray microscopy with Fresnel zone plates reaches 40 nm Rayleigh resolution. Appl Phys Lett 92:103119
12. Chen YT, Chen TY, Yi JM, Chu YS, Lee WK, Wang CL, Kempson IM, Hwu Y, Gajdosik V, Margaritondo G (2011) Hard x-ray Zernike microscopy reaches 30 nm resolution. Opt Lett 36:1269–1271
13. Chen YT, Lo TN, Chu YS, Yi J, Liu CJ, Wang JY, Wang CL, Chiu CW, Hua TE, Hwu Y, Shen Q, Yin GC, Liang KS, Lin HM, Je JH, Margaritondo G (2008) Full-field hard x-ray microscopy below 30 nm: a challenging nanofabrication achievement. Nanotechnology 19:395302
14. Chen TY, Chen YT, Wang CL, Kempson IM, Lee WK, Chu YS, Hwu Y, Margaritondo G (2011) Full-field microimaging with 8 keV X-rays achieves a spatial resolutions better than 20 nm. Opt Express 19:19919–19924
15. Meuli R, Hwu Y, Je JH, Margaritondo G (2004) Synchrotron radiation in radiology: radiology techniques based on synchrotron sources. Eur Radiol 14:1550–1560
16. Hwu Y, Tsai WL, Chang HM, Yeh HI, Hsu PC, Yang YC, Su YT, Tsai HL, Chow GM, Ho PC, Li SC, Moser HO, Yang P, Seol SK, Kim CC, Je JH, Stefanekova E, Groso A, Margaritondo G (2004) Imaging cells and tissues with refractive index radiology. Biophys J 87:4180–4187
17. Sharma P, Singh A, Brown SC, Bengtsson N, Walter GA, Grobmyer SR, Iwakuma N, Santra S, Scott EW, Moudgil BM (2010) Multimodal nanoparticulate bioimaging contrast agents. Methods Mol Biol 624:67–81
18. Lu S, Xu X, Zhao W, Wu W, Yuan H, Shen H, Zhou C, Li LS, Ma L (2010) Targeting of embryonic stem cells by peptide-conjugated quantum dots. PLoS One 5:e12075
19. Schluep T, Hwang J, Hildebrandt IJ, Czernin J, Choi CH, Alabi CA, Mack BC, Davis ME (2009) Pharmacokinetics and tumor dynamics of the nanoparticle IT-101 from PET imaging and tumor histological measurements. Proc Natl Acad Sci U S A 106:11394–11399
20. Smirnov P, Lavergne E, Gazeau F, Lewin M, Boissonnas A, Doan BT, Gillet B, Combadiere C, Combadiere B, Clement O (2006) In vivo cellular imaging of lymphocyte trafficking by MRI: a tumor model approach to cell-based anticancer therapy. Magn Reson Med 56:498–508
21. Bui T, Stevenson J, Hoekman J, Zhang S, Maravilla K, Ho RJ (2010) Novel Gd nanoparticles enhance vascular contrast for high-resolution magnetic resonance imaging. PLoS One 5:e13082
22. Markov DE, Boeve H, Gleich B, Borgert J, Antonelli A, Sfara C, Magnani M (2010) Human erythrocytes as nanoparticle carriers for magnetic particle imaging. Phys Med Biol 55:6461–6473
23. Tholouli E, Sweeney E, Barrow E, Clay V, Hoyland JA, Byers RJ (2008) Quantum dots light up pathology. J Pathol 216:275–285
24. Medintz IL, Uyeda HT, Goldman ER, Mattoussi H (2005) Quantum dot bioconjugates for imaging, labelling and sensing. Nat Mater 4:435–446
25. Niidome T, Akiyama Y, Shimoda K, Kawano T, Mori T, Katayama Y, Niidome Y (2008) In vivo monitoring of intravenously injected gold nanorods using near-infrared light. Small 4:1001–1007
26. Hahn MA, Singh AK, Sharma P, Brown SC, Moudgil BM (2010) Nanoparticles as contrast agents for in-vivo bioimaging: current status and future perspectives. Anal Bioanal Chem 399:3–27
27. Liu CJ, Wang CH, Chien CC, Yang TY, Chen ST, Leng WH, Lee CF, Lee KH, Hwu Y, Lee YC, Cheng CL, Yang CS, Chen YJ, Je JH, Margaritondo G (2008) Enhanced x-ray irradiation-induced cancer cell damage by gold nanoparticles treated by a new synthesis method of polyethylene glycol modification. Nanotechnology 19:295104
28. Wang CH, Liu CJ, Chien CC, Chen HT, Hua TE, Leng WH, Chen HH, Kempson IM, Hwu Y, Hsiao M, Lai TC, Wang JL, Yang CS, Lin HM, Chen YJ, Margaritondo G (2011) X-ray synthesized PEGylated (polyethylene glycol coated) gold nanoparticles in mice strongly accumulate in tumors. Mater Chem Phys 126:352–356
29. Cai XQ, Wang CL, Chen HH, Chien CC, Lai SF, Chen YY, Hua TE, Kempson IM, Hwu Y, Yang CS, Margaritondo G (2010) Tailored Au nanorods: optimizing functionality, controlling the aspect ratio and increasing biocompatibility. Nanotechnology 21:335604
30. Lai SF, Chen WC, Wang CL, Chen HH, Chen ST, Chien CC, Chen YY, Hung WT, Cai X, Li E, Kempson IM, Hwu Y, Yang CS, Tok ES, Tan HR, Lin M, Margaritondo G (2011) One-pot tuning of Au nucleation and growth: from nanoclusters to nanoparticles. Langmuir 27:8424–8429

31. Liu CJ, Wang CH, Chen ST, Chen HH, Leng WH, Chien CC, Wang CL, Kempson IM, Hwu Y, Lai TC, Hsiao M, Yang CS, Chen YJ, Margaritondo G (2010) Enhancement of cell radiation sensitivity by pegylated gold nanoparticles. Phys Med Biol 55:931–945
32. Hainfeld JF, Slatkin DN, Smilowitz HM (2004) The use of gold nanoparticles to enhance radiotherapy in mice. Phys Med Biol 49: N309–N315
33. Goel R, Shah N, Visaria R, Paciotti GF, Bischof JC (2009) Biodistribution of TNF-alpha-coated gold nanoparticles in an in vivo model system. Nanomedicine (London) 4:401–410
34. Moghimi SM, Hunter AC, Murray JC (2001) Long-circulating and target-specific nanoparticles: theory to practice. Pharmacol Rev 53:283–318
35. Owens DE 3rd, Peppas NA (2006) Opsonization, biodistribution, and pharmacokinetics of polymeric nanoparticles. Int J Pharm 307:93–102
36. Baish JW, Stylianopoulos T, Lanning RM, Kamoun WS, Fukumura D, Munn LL, Jain RK (2011) Scaling rules for diffusive drug delivery in tumor and normal tissues. Proc Natl Acad Sci U S A 108:1799–1803
37. Alexis F, Pridgen E, Molnar LK, Farokhzad OC (2008) Factors affecting the clearance and biodistribution of polymeric nanoparticles. Mol Pharm 5:505–515
38. Alberola AP, Rädler JO (2009) The defined presentation of nanoparticles to cells and their surface controlled uptake. Biomaterials 30:3766–3770
39. Aggarwal P, Hall JB, McLeland CB, Dobrovolskaia MA, McNeil SE (2009) Nanoparticle interaction with plasma proteins as it relates to particle biodistribution, biocompatibility and therapeutic efficacy. Adv Drug Deliv Rev 61:428–437
40. Todd ME, Tokito MK (1981) Improved ultrastructural detail in tissues fixed with potassium permanganate. Stain Technol 56:335–342
41. Sutton JS (1967) Potassium permanganate staining of ultrathin sections for electron microscopy. J Ultrastruct Mol Struct Res 21:424–429
42. Wang CH, Chien CC, Yu YL, Liu CJ, Lee CF, Chen CH, Hwu Y, Yang CS, Je JH, Margaritondo G (2007) Structural properties of 'naked' gold nanoparticles formed by synchrotron X-ray irradiation. J Synchrotron Radiat 14:477–482
43. Wang CH, Hua TE, Chien CC, Yu YL, Yang TY, Liu CJ, Leng WH, Hwu Y, Yang YC, Kim CC, Je JH, Chen CH, Lin HM, Margaritondo G (2007) Aqueous gold nanosols stabilized by electrostatic protection generated by X-ray irradiation assisted radical reduction. Mater Chem Phys 106:323–329
44. Wang CH, Liu CJ, Wang CL, Hua TE, Obliosca JM, Le KH, Hwu Y, Yang CS, Liu RS, Lin HM, Je JH, Margaritondo G (2008) Optimizing the size and surface properties of polyethylene glycol (PEG)-gold nanoparticles by intense x-ray irradiation. J Phys D Appl Phys 41:195301
45. Metscher BD (2009) MicroCT for comparative morphology: simple staining methods allow high-contrast 3D imaging of diverse non-mineralized animal tissues. BMC Physiol 9:11
46. Chen YT, Lo TN, Chiu CW, Wang JY, Wang CL, Liu CJ, Wu SR, Jeng ST, Yang CC, Shiue J, Chen CH, Hwu Y, Yin GC, Lin HM, Je JH, Margaritondo G (2008) Fabrication of high-aspect-ratio Fresnel zone plates by e-beam lithography and electroplating. J Synchrotron Radiat 15:170–175
47. Lo TN, Chen YT, Liu CJ, Chang WD, Lai TY, Wu HJ, Lin IK, Su CI, Shew BY, Je JH, Marganitondo G, Hwu Y (2007) Using e-beam and x-ray lithography techniques to fabricate zone plates for hard x-ray. In: Choi JY, Rah S (eds) Synchrotron Radiation Instrumentation, Pts 1 and 2, vol 879. AIP Conference Proceedings. American Institute of Physics, New York, pp 1466–1469
48. Chien CC, Tseng PY, Chen HH, Hua TE, Chen ST, Chen YY, Leng WH, Wang CH, Hwu Y, Yin GC, Liang KS, Chen FR, Chu YS, Yeh HI, Yang YC, Yang CS, Zhang GL, Je JH, Margaritondo G (2012) Imaging cells and sub-cellular structures with ultrahigh resolution full-field X-ray microscopy. Biotechnol Adv. doi:10.1016/j.biotechadv.2012.04.005
49. Cho W-S, Cho M, Jeong J, Choi M, Han BS, Shin H-S, Hong J, Chung BH, Jeong J, Cho M-H (2010) Size-dependent tissue kinetics of PEG-coated gold nanoparticles. Toxicol Appl Pharmacol 245:116–123
50. Romberg B, Hennink W, Storm G (2008) Sheddable Coatings for Long-Circulating Nanoparticles. Pharm Res 25:55–71
51. Chien CC, Chen HH, Lai SF, Wu KC, Cai X, Hwu Y, Petibois C, Chu YS, Margaritondo G (2012) Gold nanoparticles as high-resolution X-ray imaging contrast agents for the analysis of tumor-related micro-vasculature. J Nanobiotechnology 10:10
52. Wu SR, Chen ST, Chu YS, Conley R, Bouet N, Chien CC, Chen HH, Lin CH, Tung HT, Chen YS, Margaritondo G, Je JH, Hwu Y (2012) Nanoresolution radiology of neurons. J Phys D Appl Phys 45:242001